Nanotechnology

PAPER

Multimodal atomic force microscopy with optimized higher eigenmode sensitivity using on-chip piezoelectric actuation and sensing

Nanotechnology 30 (2019) 085503 (11pp) https://doi.org/10.1088/1361-6528/aae40b

Multimodal atomic force microscopy with optimized higher eigenmode sensitivity using on-chip piezoelectric actuation and sensing

Michael G Ruppert[1,3], **Steven I Moore**[1], **Michal Zawierta**[2], **Andrew J Fleming**[1], **Gino Putrino**[2] and **Yuen K Yong**[1]

[1] The University of Newcastle, Callaghan NSW 2308, Australia
[2] The University of Western Australia, Perth WA 6009, Australia

E-mail: michael.ruppert@newcastle.edu.au

Received 15 August 2018, revised 17 September 2018
Accepted for publication 25 September 2018
Published 2 January 2019

Abstract

Atomic force microscope (AFM) cantilevers with integrated actuation and sensing provide several distinct advantages over conventional cantilever instrumentation. These include clean frequency responses, the possibility of down-scaling and parallelization to cantilever arrays as well as the absence of optical interference. While cantilever microfabrication technology has continuously advanced over the years, the overall design has remained largely unchanged; a passive rectangular shaped cantilever design has been adopted as the industry wide standard. In this article, we demonstrate multimode AFM imaging on higher eigenmodes as well as bimodal AFM imaging with cantilevers using fully integrated piezoelectric actuation and sensing. The cantilever design maximizes the higher eigenmode deflection sensitivity by optimizing the transducer layout according to the strain mode shape. Without the need for feedthrough cancellation, the read-out method achieves close to zero actuator/sensor feedthrough and the sensitivity is sufficient to resolve the cantilever Brownian motion.

Keywords: atomic force microscopy, piezoelectric actuation and sensing, microelectromechanical systems (MEMS), multifrequency AFM, feedthrough, noise analysis

(Some figures may appear in colour only in the online journal)

1. Introduction

Micro and nano precision mechatronic systems have significantly enabled the steady growth of nanotechnology over the past three decades. They are situated at the heart of a variety of instruments for manipulation and interrogation at the nanoscale, such as atomic force microscopes (AFM) [1], scanning tunneling microscopes [2], scanning lithography systems [3] and probe-based data storage systems [4].

A key component of these instruments is a microcantilever which forms the physical link between the sample under investigation and the measurable quantity. It has served as a key nano-interrogation tool contributing to major innovations in a number of industrial applications and research fields including nanometrology [5], semiconductor manufacturing [6], material science [7] and bio-nanotechnology [8].

While cantilever microfabrication technology has continuously advanced over the years, the overall design has remained largely unchanged; a passive rectangular cantilever has been adopted as the industry wide standard. Consequently, conventional cantilever instrumentation requires external piezo-acoustic excitation [9] as well as an external optical deflection sensor [10]. Both of these components are not optimal for trends in multifrequency AFM technology

[3] Author to whom any correspondence should be addressed.

which can extend the imaging information beyond the topography to a range of nano-mechanical properties including sample stiffness, elasticity and adhesiveness [11–13]. In contrast, active cantilevers with integrated actuation and sensing on the chip level provide several distinct advantages over conventional cantilever instrumentation [14]. These include 'clean' frequency responses that do not include structural modes of the mounting system [15], the possibility of down-scaling [16], single-chip AFM implementations [17, 18], parallelization to cantilever arrays [19] as well as the absence of optical interference [20].

A number of integrated actuation methods have been developed over the years to replace the piezo-acoustic excitation [21–23], however only electro-thermal [24] or piezoelectric actuation [25] can be directly integrated on the cantilever chip. Compared to the optical beam deflection sensor, strain-based deflection measurements such as piezoelectric [26] and piezoresistive sensing [27] yield a much more compact form factor, and increased sensitivity for smaller cantilever dimensions [28–30] and higher order eigenmodes [31].

Utilizing piezoelectric layers for both actuation and sensing is a promising avenue when trying to minimize the number of microelectromechanical systems (MEMS) fabrication steps. However, complete electrical isolation between the sense and drive electrodes is difficult to incorporate resulting in parasitic coupling and a potentially large feedthrough path from actuation to sensing [32, 33]. Since the feedthrough adds to the sensor signal, it can entirely conceal the signal originating from the motion of the structure. As a result, feedthrough cancellation techniques have to be employed in order to cancel the parasitic feedthrough [15, 18, 34–36]. While these techniques can recover a buried resonance peak, tuning can be cumbersome and the additive nature of the cancellation modifies the cantilever system dynamics and degrades noise performance.

In this work, a cantilever design with integrated piezoelectric actuation and sensing is presented which enables multimode AFM imaging without the need for feedthrough cancellation. Due to the ability to design the location and layout of the piezoelectric transducers, the deflection sensitivity of the first two eigenmodes is optimized while also providing separated actuators and sensors. A detailed analysis of the electrical circuit noise is performed both in simulation and in experiment. The low noise of the proposed method allows the detection of Brownian motion at the first eigenmode of the cantilever. The entire system is demonstrated to perform single-mode AFM imaging on a SiC sample as well as bimodal AFM imaging on a polymer blend.

2. Cantilever design and instrumentation

2.1. Cantilever design

The cantilever geometry chosen for this work is a stepped rectangular design which has the benefit of closely spaced higher eigenmodes [37]. The cantilever consists of a wider section with dimensions of 500 μm × 400 μm and a smaller section with dimensions of 100 μm × 400 μm. A photo of the fabricated cantilever is shown in figure 1. The wire-bonding pads labeled A and S are used for actuation and sensing. The ground trace is run between the signal traces and piezoelectric areas in order to minimize the actuator-sensor feedthrough [38].

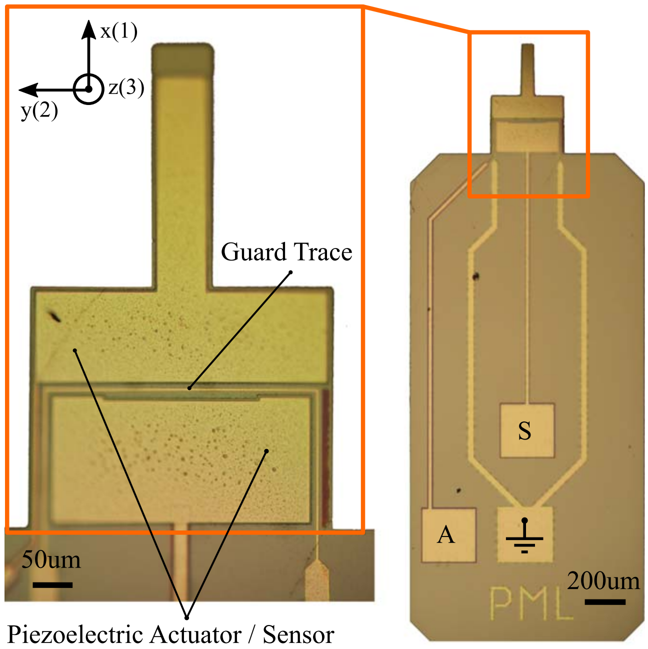

Figure 1. Photo of fabricated bimodal piezoelectric MEMS cantilever with integrated piezoelectric actuation and sensing.

A piezoelectric transducer generates mechanical stress/strain in response to an applied electric field and vice versa. This behavior is described by the IEEE standard on piezoelectricity [39] and for the pure bending case can be written with the two scalar constitutive equations (axis definition as per figure 1)

$$\epsilon_1 = \frac{1}{Y}\sigma_1 + d_{31}E_3, \tag{1}$$

$$D_3 = d_{31}\sigma_1 + \xi_{33}E_3 \tag{2}$$

with Young's modulus $Y\,(\mathrm{N\,m^{-2}})$, piezoelectric $d\,(\mathrm{m\,V^{-1}})$ and dielectric $\xi\,(\mathrm{F\,m^{-1}})$ material constants, applied stress $\sigma\,(\mathrm{N\,m^{-2}})$, applied electrical field $E\,(\mathrm{V\,m^{-1}})$ and the dependent variables resulting strain $\epsilon\,(\mathrm{m\,m^{-1}})$ and resulting electrical displacement $D\,(\mathrm{C\,m^{-2}})$. When used as a sensor, a charge is generated on the electrode surfaces of the piezoelectric material [40]

$$Q = \int_A D_3 dA. \tag{3}$$

For an Euler–Bernoulli beam approximation, the charge can be calculated from the integral of the second derivative of the mode shape

$$Q = \int_A d_{31}\sigma_s(x)dA = -\frac{d_{31}Yt}{2}\int_A z''(x)dA, \tag{4}$$

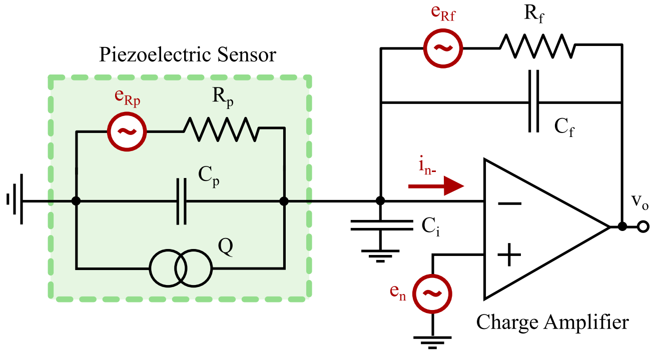

Figure 2. Electrical circuit configuration of the piezoelectric charge amplifier with the four electrical noise sources: Johnson noise in resistors R_p and R_f, op-amp voltage noise e_n and op-amp current noise i_{n-}.

where $\sigma_s(x)$ is the surface stress at the position x along the cantilever, t is the total cantilever thickness. The charge output can be stated as a function of the tip deflection using the static bending case approximation [41] (compare appendix A)

$$Q = \frac{3}{4L} d_{31} t w Y z(L) \tag{5}$$

assuming a piezoelectric sensor over the full cantilever width w and length L. For non-Euler–Bernoulli beams like the cantilever in this work, Mindlin plate theory is used to obtain a finite element model to perform modal analysis. The charge response of each finite element is calculated as [42]

$$Q = \frac{d_{31} t}{2} \int_x \int_y \frac{\partial \theta_y(x, y)}{\partial x} - \frac{\partial \theta_x(x, y)}{\partial y} dx dy, \tag{6}$$

where $\theta_{x,y}(x, y)$ are the rotations of the normal of the cantilevers neutral plane around the x-axis and y-axis, respectively. As such, higher eigenmode deflection sensitivities can be maximized by placing individual piezoelectric regions on areas where the charge response of the finite elements of a flexural mode do not change the sign [31]. This approach avoids the cancellation of charges with opposite sign, which would lead to reduced actuator gain and sensor sensitivity. If this design procedure is applied for the first and second flexural eigenmodes, a piezoelectric layer configuration as shown in figure 1 is obtained. This configuration is optimal for transduction of the first two eigenmodes of the cantilever while providing separated actuators and sensors, enabling single mode and bimodal AFM imaging.

2.2. Cantilever instrumentation

The piezoelectric actuator can be driven directly by an input voltage source. The piezoelectric sensor is instrumented with a first stage charge-mode amplifier circuit shown in figure 2 which amplifies the charge generated by the strain-dependent piezoelectric voltage source V_p on the piezoelectric capacitance C_p [43]. The benefit of this circuit is that the high-frequency sensor gain only depends on the feedback capacitance C_f and is independent of the input capacitance at the op-amp. The circuit forms a high-pass filter from piezoelectric charge to first stage output voltage

$$H(s) = \frac{V_o(s)}{Q(s)} = \frac{-R_f s}{R_f C_f s + 1}, \tag{7}$$

where the high-frequency charge-to-voltage gain is $1/C_f$ and the corner frequency is given by $f_c = (2\pi R_f C_f)^{-1}$.

2.3. Circuit noise analysis

Throughout the following analysis and for the remainder of the paper, we refer to $N_{x,y}(f) = \sqrt{S_{x,y}(f)}$ as the noise spectral density of the signal x due to a process y as a function of frequency f. The electrical noise in the charge amplifier readout circuit is dictated by four major noise sources shown in figure 2: Johnson thermal noise in the piezo resistor R_p and amplifier feedback resistor R_f, op-amp voltage noise e_n and op-amp current noise i_{n-}. The noise sources can all be referred to an equivalent op-amp input noise voltage (RTI) or referred to output noise (RTO) by multiplying the RTI noise with the noise gain G_n of the circuit

$$G_n(s) = 1 + \frac{C_f || R_f}{C_s || R_p} = 1 + \frac{R_f}{R_p} \frac{C_s R_p s + 1}{C_f R_f s + 1}, \tag{8}$$

where $C_s = C_p + C_i$ is the total input capacitance seen by the op-amp inverting input. The noise gain magnitude is

$$|G_n(s)| = \begin{cases} 1 + \frac{R_f}{R_p} & f \ll f_c \\ 1 + \frac{C_s}{C_f} & f \gg f_c. \end{cases}$$

The individual output noise spectral densities can be written as

$$N_{v_o,e_n}(f) = e_{nv} |G_n(s)|, \tag{9}$$

$$N_{v_o,i_n}(f) = i_{n-} |Z_f(s)|, \tag{10}$$

$$N_{v_o,R_p}(f) = \left(\frac{e_{Rp}}{R_p} \right) |Z_f(s)|, \tag{11}$$

$$N_{v_o,R_f}(f) = \left(\frac{e_{Rf}}{R_f} \right) |Z_f(s)|, \tag{12}$$

where the feedback impedance is given by

$$Z_f(s) = R_f || C_f = \frac{R_f}{R_f C_f s + 1}. \tag{13}$$

The total output voltage noise spectral density is then obtained from

$$N_{v_o}(f) = \sqrt{N_{v_o,e_n}^2 + N_{v_o,i_n}^2 + N_{v_o,R_p}^2 + N_{v_o,R_f}^2}. \tag{14}$$

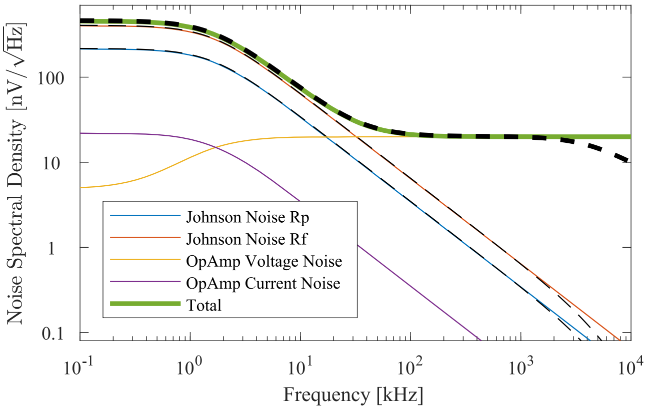

Figure 3. Theoretical output voltage noise spectral densities of the charge-mode amplifier noise sources and LTspice simulations in black dashed lines: Johnson Noise in resistors R_p (11) and R_f (12), op-amp voltage noise (9) and current noise (10) resulting in the total output voltage noise spectral density (14).

These equations have been evaluated for a measured piezoelectric impedance of the cantilever with $R_p = 35\,\mathrm{M}\Omega$ and $C_p = 38\,\mathrm{pF}$. The feedback impedance values chosen were $R_f = 10\,\mathrm{M}\Omega$ and $C_f = 10\,\mathrm{pF}$ resulting in a charge-to-voltage gain of 220 dB and cut-off frequency of 1.59 kHz. The results were compared with LTspice simulations using the JFET op-amp OPA827 with $e_n = 3.8\,\mathrm{nV}/\sqrt{\mathrm{Hz}}$, $i_{n-} = 2.2\,\mathrm{fA}/\sqrt{\mathrm{Hz}}$ and $C_i = 4.5\,\mathrm{pF}$.

The results are shown in figure 3. It can be seen that the theoretical equations predict the total noise spectral density as well as the Johnson noise from the resistors accurately. At low frequencies, the noise floor is dictated by the Johnson noise in the feedback resistor R_f. At high frequencies, the noise floor is dictated by the op-amp voltage noise multiplied by the high-frequency noise gain $1 + \frac{C_s}{C_f}$, which results in $19.95\,\mathrm{nV}/\sqrt{\mathrm{Hz}}$. At the resonance frequency of the first mode ($f = 36\,\mathrm{kHz}$), the total noise is $28.71\,\mathrm{nV}/\sqrt{\mathrm{Hz}}$. Assuming post-amplification stages with a combined gain of 100, the total expected electrical noise floor is approximately $2.9\,\mu\mathrm{V}/\sqrt{\mathrm{Hz}}$.

2.4. Electrical circuit optimization

The deflection noise density (at the resonance frequency) is a function of the feedback capacitance C_f and feedback resistance R_f. The choice of these components is non-trivial since they determine the high-frequency noise gain, the signal gain as well as the high-pass filter cut-off frequency (7) which needs to be maintained well below the first mode resonance frequency of the cantilever. Therefore, it is advantageous to optimize C_f and R_f to minimize the deflection noise density due to electrical noise which is given by

$$N_e(f) = \frac{N_{v_o}(f)}{\Psi_{\mathrm{PZE}}}, \tag{15}$$

where Ψ_{PZE} is the piezoelectric deflection sensitivity (see appendix A). For the simulation, the experimentally determined piezoelectric deflection sensitivity (table 1) has been used.

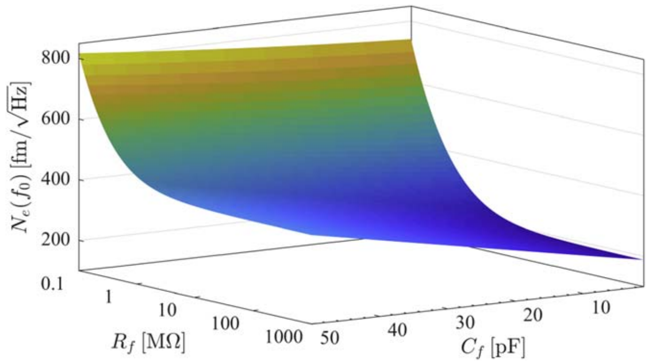

Figure 4. Total deflection noise density of the charge-mode read-out circuit at the fundamental resonance frequency as a function of feedback capacitance and resistance.

Table 1. Summary of the modal piezoelectric gains and sensitivities.

	Actuation gain (nm mV^{-1})	Deflection sensitivity (mV nm^{-1})
Mode 1	6.038	9.5021
Mode 2	2.719	10.4328

A plot of $|N_e(f_0)|$ as a function of the feedback impedance parameters is shown in figure 4. For a given fixed piezoelectric capacitance and input capacitance of the op-amp, minimizing N_e is achieved by minimizing the feedback capacitance and maximizing the feedback resistance while maintaining the frequency constraint $10\,fc < f_0$ of the high-pass filter characteristic (7). Due to challenges with implementing very high resistance and capacitance values that approach circuit parasitics, $R_f = 10\,\mathrm{M}\Omega$ and $C_f = 10\,\mathrm{pF}$ was chosen but these could be further optimized in future designs. In the pass band of the charge sensor $f \gg f_c$, N_e (15) is dominated by the contribution arising from the op-amp voltage noise term (9)

$$|N_e(f \gg f_c)| \propto \frac{e_n(1 + \frac{C_s}{C_f})}{\frac{1}{C_f}} = e_n(C_s + C_f). \tag{16}$$

Minimizing N_e is achieved by minimizing the feedback capacitance and all op-amp input capacitances including the piezoelectric capacitance as the generated charge is not a function of the piezoelectric capacitance (5).

3. Experimental results

3.1. Device fabrication

3.1.1. Cantilever fabrication. The piezoelectric cantilevers were fabricated using the rapid five mask MEMS prototyping process PiezoMUMPS® (MEMSCAP Inc.) [44]. The process features a 400 μm silicon substrate, a device layer of single-crystal-silicon with a thickness of 10 μm, a 0.5 μm layer of piezoelectric aluminum-nitrate (AlN) and a 20 nm chrome/1 μm aluminum metal stack layer for electrical connections.

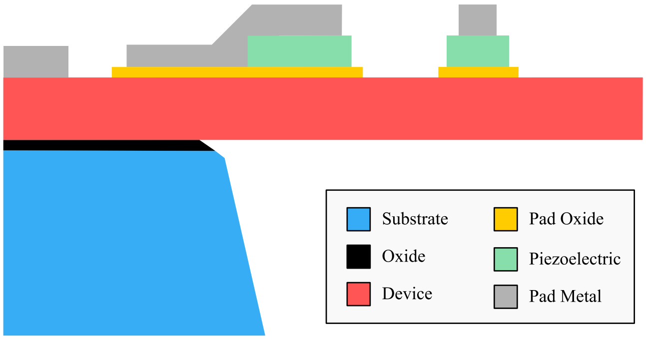

Figure 5. Schematic of the PiezoMUMPS® five mask microfabrication process (not to scale).

A cross-section schematic of the process is shown in figure 5. The top surface of the device layer is doped by depositing a phosphosilicate glass layer and annealing in argon and is subsequently used as the device common ground return path. Electrical insulation between the signal tracks and ground is provided by a 1 μm pad oxide layer.

3.1.2. Tip fabrication. As the PiezoMUMPS® process does not allow for the inclusion of sharp tips at the cantilever end, two types of post-fabricated tips have been employed as shown in figure 6: welding of a pre-fabricated silicon tip to the cantilever and focused ion beam (FIB) induced deposition of a new Tungsten tip. Both solutions were implemented using a FEI Helios Nanolab G3 CX DualBeam FIB/SEM.

In the first approach, commercially available silicon AFM cantilevers were used as a source of sharp, well-defined tips. In the first step, the cantilever tip is cut out in a U-shaped pattern using FIB milling while being attached to a micromanipulator needle. After transferring the removed tip and aligning it on top of the PiezoMUMPS® cantilever, FIB Platinum welding is used to permanently fix the tip. SEM images of this workflow are shown in figure 6.

In the second approach, direct FIB deposition of Tungsten is used to form single or multi-segment tips which are subsequently sharpened using tilted FIB milling. The diameter of the single segment tips is approximately $d = 250$ nm and the height $h = 12$ μm. The diameter of the three segment tips is approximately $d = 2$ μm, 1 μm, 200 nm and the height $h = 12$ μm. SEM images of these tips are shown in figure 6.

3.2. Sensor implementation and experimental setup

The fabricated charge-mode amplifier read-out circuit with a 3D-printed cantilever holder for a Horiba XploRA Nano Raman-AFM system is shown in figure 7. The read-out circuit contains on-board low-noise power supplies (± 5 V linear regulators TPS7A4901 and TPS7A3001), a first stage charge amplifier (Texas Instruments OPA827 low-noise JFET op-amp) and additional low-noise post amplification stages (Texas Instruments OPA2211 low-noise precision op-amp) for additional gain. The fabricated MEMS cantilevers are glued directly onto the PCB in order to achieve the best performance. Guarding the highly sensitive charge input trace

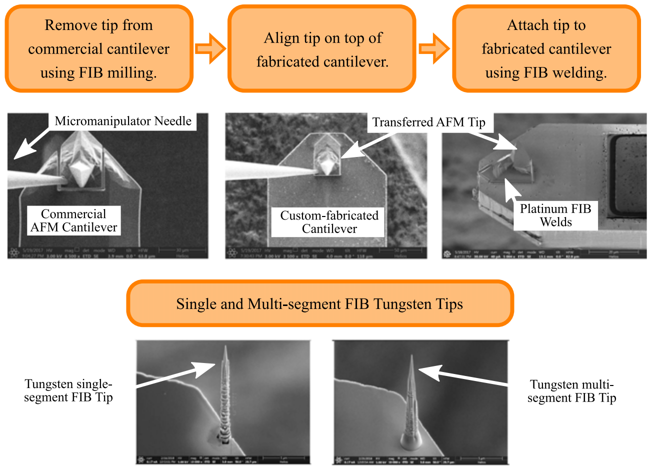

Figure 6. SEM images of the workflow for post-fabrication of FIB welded tips and SEM images of fabricated single/multisegment FIB tungsten tips.

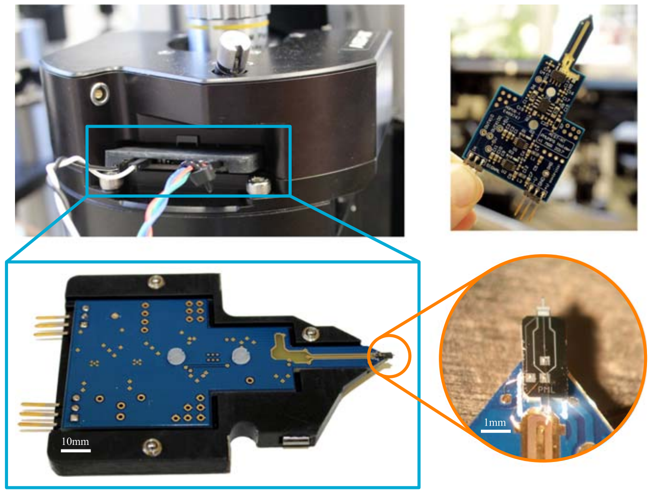

Figure 7. Photos of the implemented charge-mode amplifier read-out circuit for a Horiba XploRA Nano Raman-AFM system.

through all levels of the PCB and into the first stage op-amp package is necessary to achieve a low parasitic capacitance to the input which in turn results in minimal feedthrough.

3.3. Modal analysis and self-sensing frequency responses

The frequency response of the piezoelectric cantilever is measured with a laser Doppler vibrometer (Polytec MSA-100-3D) and using the integrated piezoelectric sensor. The displacement response is obtained by broad-band periodic chirp excitation and integration of the velocity measurement in the frequency domain. The charge response is measured by performing a frequency sweep with a lock-in amplifier (Zurich Instruments HF2LI). Both results are directly compared in figure 8 by aligning the charge response to the displacement response on the first mode. The dynamic range of the charge frequency response is similar to the direct displacement measurement which implies a very low actuator/sensor feedthrough. This is further evident in the close-up view of the first and second mode which show a full 180°

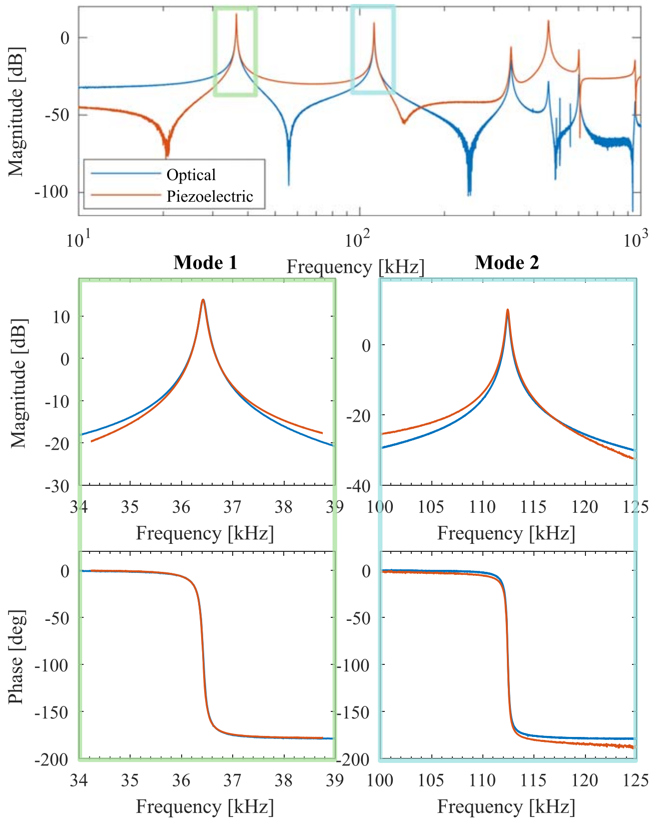

Figure 8. Frequency response of the piezoelectric cantilever measured with a laser Doppler vibrometer (MSA-100-3D) and using the integrated piezoelectric charge sensor.

phase transition and a very close match to the true displacement response. Another indicator for a low actuator/sensor feedthrough is the location of the complex zero pair leading up to the first eigenmode. This effect is explained by a small amount of parasitic capacitance between actuator and sensor causing a residual amount of feedthrough charge with opposite sign to the motional charge [38].

The modal sensitivities are found by exciting each mode with a pure sine tone and measuring the displacement response optically and with the piezoelectric charge sensor. Table 1 summarizes the displacement (actuation) and charge (sensing) sensitivities.

3.4. Noise performance

3.4.1. Thermal noise measurement. The noise performance of the piezoelectric sensor implementation is assessed by measuring the Brownian motion at room temperature and recording the corresponding thermal noise spectrum around the fundamental eigenmode of the cantilever. The total measured deflection noise density is

$$N_d(f) = \sqrt{N_z^2(f) + N_e^2(f)}, \tag{17}$$

where N_e is the deflection noise density due to electrical noise (15) and N_z is the thermomechanical deflection noise density of the fundamental mode of the cantilever as observed by the

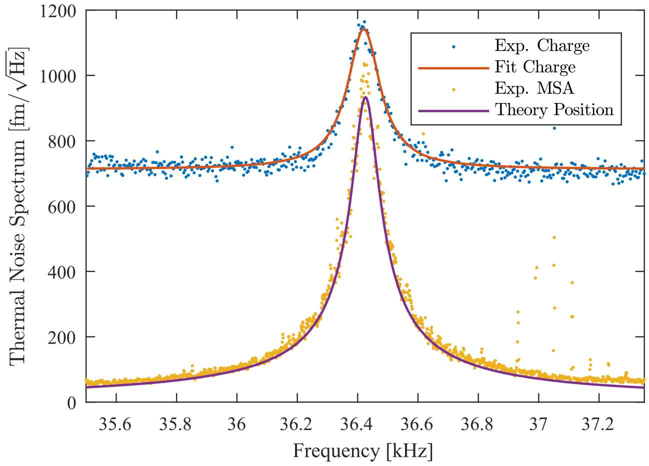

Figure 9. Thermal noise spectrum of the fundamental mode of the piezoelectric cantilever measured with the integrated charge sensor (Exp. Charge) and with a laser Doppler vibrometer (Exp. MSA). A Lorentzian fit to the charge response (Fit Charge) and the theoretical position power spectral density of the harmonic oscillator (see appendix B) (Theory Position) is also shown.

piezoelectric sensor (see appendix B)

$$N_z(\omega) = \sqrt{0.8175\frac{4k_BT}{k\omega_0 Q}\frac{1}{\left(1-\frac{\omega^2}{\omega_0^2}\right)^2+\frac{\omega^2}{\omega_0^2Q^2}}}, \tag{18}$$

where k_B, T, k, ω_0, Q are the Boltzman constant, absolute temperature, dynamic stiffness, resonance frequency and quality factor. The cantilever parameters are identified from a Lorentzian function fit to the velocity power spectrum obtained from the laser Doppler vibrometer measurement [45] and are determined as $k = 33.67$ N m^{-1}, $Q = 369.8$, $\omega_0 = 2\pi 36.42$ kHz. Similarly, the cantilever spring constant can be identified from the piezoelectric thermal noise spectrum which yields $k = 30.04$ N m^{-1} using

$$k = \frac{k_BT\Psi_{\text{PZE}}^2}{P}, \tag{19}$$

where P is the positional noise power in units of (V^2) isolated in the fundamental resonance mode (area underneath the thermal noise peak) and Ψ_{PZE} is the piezoelectric deflection sensitivity stated in table 1. The measurement is within acceptable experimental tolerance levels but is very sensitive to the displacement calibration factor.

The deflection noise densities measured with the piezoelectric sensor and with the laser Doppler vibrometer (Polytec MSA-100-3D, noise floor 30 fm/$\sqrt{\text{Hz}}$) are shown in figure 9. Also shown is a Lorentzian function fit to the charge response which estimates the white noise floor to be 712 fm/$\sqrt{\text{Hz}}$ using the first mode charge sensitivity state in table 1, or 6.77 μV/$\sqrt{\text{Hz}}$ in the voltage domain. This value is comparable to practical OBD sensor systems in commercial AFMs which achieve 100–1000 fm/$\sqrt{\text{Hz}}$ [46]. At resonance, the peak value is 1141 fm/$\sqrt{\text{Hz}}$. Note that the difference between the spectra is due only to the differences in the noise floor between the two sensors, according to (17). That is, the thermomechanical noise is identical. From the analytical

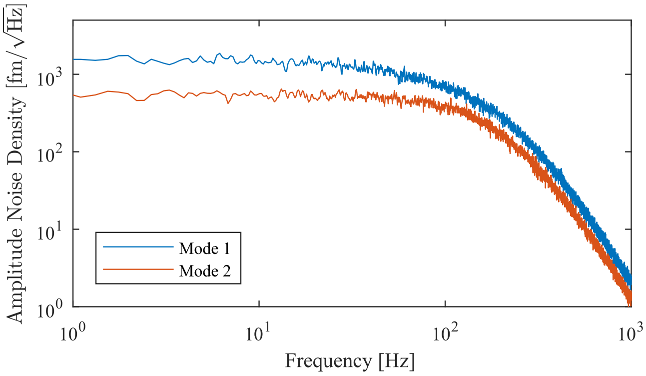

Figure 10. Demodulated amplitude noise on the first and second eigenmode at a 100 Hz demodulation bandwidth.

equations presented in section 2.3, the total noise floor of the sensor around the first mode resonance should be $2.9\ \mu\mathrm{V}/\sqrt{\mathrm{Hz}}$ assuming an OPA827 operational amplifier with post-amplification stages with a gain of 100. The increased noise floor can be explained by additional parasitic circuit elements such as an increased input capacitance and tolerances in the circuit components. In the pass-band of the charge sensor, the high-frequency noise floor is measured at $4.85\ \mu\mathrm{V}/\sqrt{\mathrm{Hz}}$ in the voltage domain.

While the noise floor of the piezoelectric charge sensor is comparable to practical OBD sensor systems in commercial AFMs, it does not yet compare to the lowest optical read-out methods reported in the literature. However, there are significant opportunities for improvement by using a piezoelectric material with a larger strain constant d_{31}. This would yield a significantly higher piezoelectric deflection sensitivity Ψ_{PZE} which scales the electrical noise floor (15).

3.4.2. Demodulated amplitude noise. The amplitude voltage noise density is obtained by actively driving the first and second eigenmode of the cantilever and demodulating the charge sensor output with a lock-in amplifier (HF2LI Zurich Instruments). The cantilever is actively driven at each mode, resulting in a deflection of 60 nm on the first mode and 27 nm on the second mode. A 4th-order low-pass filter with cut-off frequency of $f_c = 100$ Hz is used in the lock-in amplifier. Using the actively driven sensor sensitivities from table 1, amplitude deflection noise density estimates on each mode are shown in figure 10 which are obtained from the time-domain demodulated amplitude signals sampled at 14.4 kHz. From the plot, the amplitude deflection noise density on the first mode is $1113\ \mathrm{fm}/\sqrt{\mathrm{Hz}}$ and on the second mode is $505.2\ \mathrm{fm}/\sqrt{\mathrm{Hz}}$. The first mode value matches the thermal noise peak value at resonance from figure 9.

3.5. AFM imaging

The multimode piezoelectric cantilever with read-out circuit was interfaced with a Horiba XploRA Nano Raman-AFM system as shown in figure 7. Two samples were investigated: a SiC-STEP calibration sample (Ted Pella) with single step heights of 1.5 nm was imaged with the first and second eigenmode and a blend of polystyrene (PS) and polyolefin elastomer (LDPE) (Bruker, PS-LDPE-12M) was imaged in bimodal AFM using the first and second eigenmode. Due to the varying elastic moduli between the PS and LPDE regions, this sample is a widely used standard to image material contrast.

3.5.1. Imaging on higher eigenmodes on SiC-STEP sample. Single mode AFM imaging was performed using the first and second eigenmode of the piezoelectric cantilever respectively on a SiC-STEP calibration sample (Ted Pella). The results are shown in figure 11 where except for plane leveling and line fitting no other post-processing has been applied to the AFM data. Imaging on the first eigenmode was performed at a free-air amplitude of $A_{1,0} \approx 50$ nm at a setpoint of 85% and on the second eigenmode at a free-air amplitude of $A_{2,0} \approx 20$ nm at a setpoint of 90%. For both cases, good topography results are obtained of the SiC steps whereas the second mode image shows lower noise as is evident from the cross-section analysis in figure 11. This can be attributed to the higher deflection sensitivity and lower circuit noise at the second mode frequency. The lower noise on the second eigenmode allows for a small harmonic electric noise source to be visible in the topography image.

3.5.2. Bimodal imaging on PS-LDPE sample. Bimodal AFM imaging was performed using the first and second eigenmode of the piezoelectric cantilever on a PS/LPDE sample (Bruker) and are shown in figure 12. The first eigenmode free-air amplitude was set to $A_{1,0} \approx 50$ nm and the second eigenmode free-air amplitude was set to $A_{2,0} \approx 7.5$ nm. The dynamic stiffnesses of the first and second eigenmode are determined from a thermal noise calibration and are found to be $k_1 = 33.67\ \mathrm{N\ m^{-1}}$ and $k_2 = 288\ \mathrm{N\ m^{-1}}$. From the histogram plots of the phase images of the first and second eigenmode, the improved phase contrast of the second eigenmode channel is clearly visible. While the first eigenmode contrast is about $\Delta\Phi_1 = 40.8°$, the second eigenmode contrast is about $\Delta\Phi_2 = 82°$. The phase images have been shifted to zero degrees to enable a better comparison.

4. Conclusion

This paper has demonstrated cantilevers optimized for multimode operation with fully integrated piezoelectric actuation and sensing on the chip level. Previously reported limitations due to actuator/sensor feedthrough are mitigated by the inclusion of guard traces on both the circuit and MEMS device. Single mode AFM imaging on the first and second eigenmode as well as bimodal imaging using the first two eigenmodes is shown to provide adequate imaging quality. While the deflection noise sensitivity of the read-out method is not yet comparable to the lowest noise optical read-out methods in literature, optimization of the piezoelectric sensitivity constant leaves significant opportunities for improvement.

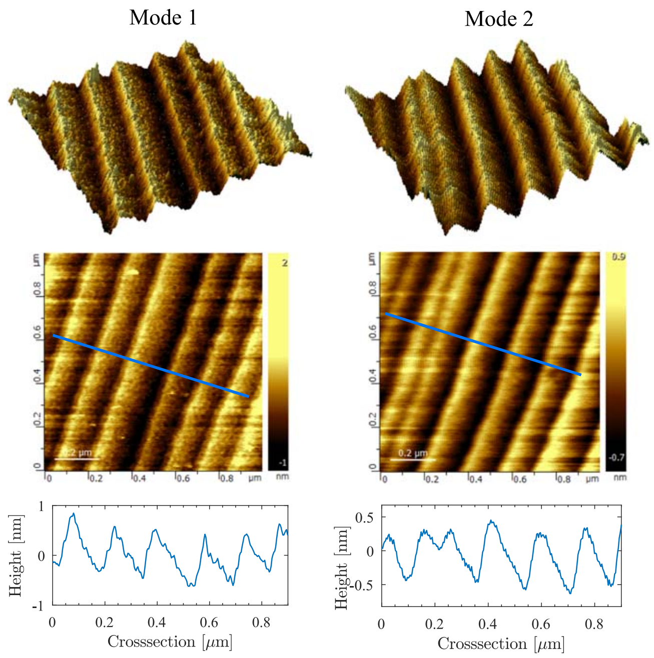

Figure 11. Single mode AFM imaging using the first and second eigenmode of the piezoelectric cantilever on a 1.5 nm SiC sample.

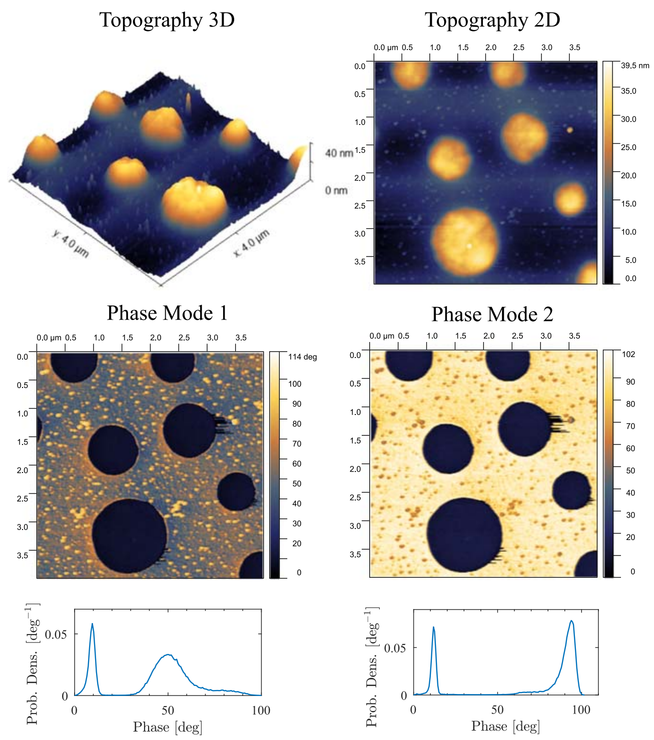

Figure 12. Bimodal AFM imaging using the first and second eigenmode of the piezoelectric cantilever on a PS/LPDE sample.

Appendix A. Charge sensitivity

The following derivation assumes a cantilevered Euler–Bernoulli such that the bending stress in x-direction is given by [41]

$$\sigma(x) = Y\epsilon(x) = -zYz''(x), \tag{A1}$$

where z is the perpendicular distance to the neutral axis and Y is the Young's modulus of the material. Here, stress is defined to be positive under elongation (tensile stress) and negative under compression (compressive stress). $z''(x)$ is the second derivative of the displacement mode shape which is related to the curvature of the beam and can be derived from the static solutions to the Euler–Bernoulli equations under a point load at the tip [41]

$$z(x) = \frac{Fx^2}{6YI}(3L - x), \tag{A2}$$

$$z'(x) = \frac{Fx}{2YI}(2L - x), \tag{A3}$$

$$z''(x) = \frac{F}{YI}(L - x). \tag{A4}$$

The displacement at the free end $x = L$, for a given point force F is given by

$$z(L) = \frac{FL^3}{3YI} = \frac{F}{k}, \tag{A5}$$

where k is the static spring constant of the cantilever. Therefore the resulting slope and second derivative as a function of the free-end deflection can be found by substituting the force

$$z'(x) = \frac{3x}{2L^3}(2L - x)z(L), \tag{A6}$$

$$z''(x) = \frac{3}{L^3}(L - x)z(L). \tag{A7}$$

The charge collected on the electrodes of the piezoelectric layer located at the surface $z = t/2$ can be determined by integrating the electrical displacement over the electrode area [40]

$$Q = \int_A D_3 dA = \int_A d_{31}\sigma_s(x) dA. \tag{A8}$$

Using $\sigma_s(x) = -t/2Yz''(x)$ and assuming a piezoelectric sensor over the full cantilever width w, the charge can be calculated as

$$Q = \frac{d_{31}tY}{2}\int_A z''(x)dA = \frac{d_{31}twY}{2}\int_x z''(x)dx. \tag{A9}$$

Assuming that the piezoelectric transducer is also over the entire length of cantilever L, the charge can be calculated as

$$Q = \frac{d_{31}twY}{2}\int_0^L z''(x)dx = \frac{d_{31}twY}{2}[z'(L) - z'(0)]. \tag{A10}$$

Since the cantilever is clamped at the base, the slope is zero $z'(0) = 0$ and therefore:

$$Q = \frac{d_{31}twY}{2}z'(L). \tag{A11}$$

Using $z'(L) = \frac{3}{2L}z(L)$, the charge as a function of tip displacement is found to be

$$Q = \frac{3}{4L}d_{31}twYz(L). \tag{A12}$$

Using the transfer function of the charge amplifier read-out circuit, the piezoelectric displacement sensitivity in units of (V m^{-1})

is given by

$$\Psi_{\mathrm{PZE}} = H(s)\frac{3d_{31}twY}{4L} \approx \frac{3d_{31}twY}{4LC_f}. \tag{A13}$$

Appendix B. Thermomechanical piezoelectric noise

B.1. Thermal vibrations

A single mode of the cantilever can be approximated by a simple harmonic oscillator for which the potential energy can be written as [47]

$$\frac{1}{2}m\omega_0^2\langle z_i^2\rangle = \frac{1}{2}k\langle z_i^2\rangle, \tag{B1}$$

where m, ω_0, k are the mass, resonance frequency, stiffness and $\langle z_i^2\rangle$ are the mean squared deflection of the oscillator [48]. The equipartition theorem states that if the system is in thermal equilibrium, the total energy of each vibrational mode (potential plus kinetic energy) has a mean value equal to $1/2k_BT$, where k_B is the Boltzman constant and T the absolute temperature [7]. Therefore, the equipartition theorem demands

$$\frac{1}{2}k\langle z_i^2\rangle = \frac{1}{2}k_BT \tag{B2}$$

and consequently the thermal noise vibrations can be stated as [48]

$$\langle z_i^2\rangle = \frac{k_BT}{k}. \tag{B3}$$

However, this expression is only true for a simple harmonic oscillator, without the assumption of a mode shape. For a cantilever, the mode shapes of each vibrational mode have to be taken into account which yields a correction factor applied to (B3). As such, the Euler–Bernoulli partial differential beam equation has to be solved to obtain the transverse deflection of a uniform and rectangular cantilever without tip-mass. The solution can be represented by separable space and time functions representing the mode shape $\Phi_i(x)$ and harmonic function $q_i(t)$ as [49]

$$z(x, t) = \sum_{i=1}^{\infty} q_i(t)\Phi_i(x). \tag{B4}$$

For a cantilevered beam, it can be shown that the mode shapes have the form [50]

$$\Phi_i(x) = (\sin\alpha_i + \sinh\alpha_i)\left[\cos\frac{\alpha_i}{L}x - \cosh\frac{\alpha_i}{L}x\right] \tag{B5}$$

$$-(\cos\alpha_i + h\cos\alpha_i)\left[\sin\frac{\alpha_i}{L}x - \sinh\frac{\alpha_i}{L}x\right] \tag{B6}$$

where α_i is the solution of the dispersion equation

$$\cos\alpha_i\cosh\alpha_i + 1 = 0, \tag{B7}$$

which is given by $\alpha_1 = 1.875$, $\alpha_2 = 4.694$, $\alpha_3 = 7.855$ for the first three modes. The deflection at the tip of the cantilever of a single mode can now be expressed as

$$z_i(L, t) = q_i(t)\Phi_i(L) \tag{B8}$$

which leads to the general expression of the mean squared deflection

$$\langle z_i^2\rangle = q_i^2\Phi_i^2(L). \tag{B9}$$

Using the Equipartition theorem, it was shown that [50]

$$q_i^2 = \frac{3k_BT}{\alpha_i^4 K(\sin\alpha_i + \sinh\alpha_i)^2} \tag{B10}$$

and

$$\Phi_i^2(L) = 4(\sin\alpha_i + \sinh\alpha_i)^2. \tag{B11}$$

Hence, the mean squared displacement at the free end for the i-th mode due to Brownian motion is [50]

$$\langle z_i^2\rangle = \frac{12}{\alpha_i^4}\frac{k_BT}{k}. \tag{B12}$$

It can be seen that the thermal vibrations rapidly decrease with increasing mode number as a function of α_i^4. For the fundamental mode $\alpha_1 = 1.875$ and

$$\langle z_1^2\rangle = 0.971\frac{k_BT}{k} \tag{B13}$$

can be used as an approximation [50].

However, the output of the piezoelectric sensor is proportional to the area integral over the second derivative of the mode shape. If the piezoelectric layer is across the entire width and length of the rectangular cantilever, the integral simplifies to

$$\int_x z''(x)dx = z'(L) \tag{B14}$$

and is hence proportional to the bending angle at the free tip. Consequently, the thermal noise observed with the piezoelectric sensor scales equally as if it was observed with the OBD sensor. The relationship between bending angle and tip deflection is given by

$$z'(L) = \frac{3}{2L}z(L), \tag{B15}$$

which leads to the mean squared virtual thermal vibrations as [50]

$$\langle z_{i*}^2\rangle = \left(\frac{2L}{3}\right)^2 q_i^2\Phi_i'(L)^2 \tag{B16}$$

$$= \left(\frac{2L}{3}\right)^2\frac{3k_BT}{K\alpha_i^4}\Phi_i'(L)^2 \tag{B17}$$

$$= \frac{16}{3\alpha_i^2}\left(\frac{\sin\alpha_i\sinh\alpha_i}{\sin\alpha_i + \sinh\alpha_i}\right)^2\frac{k_BT}{k}. \tag{B18}$$

Compared to (B12), it can be observed that the thermal vibrations decrease only as a function of α_i^2. For the fundamental mode $\alpha_1 = 1.875$ and

$$\langle z_{1*}^2\rangle = 0.8175\frac{k_BT}{k} \tag{B19}$$

can be used as an approximation [50].

B.2. Spectrum

The mean squared deflection at the end of the cantilever and the displacement power spectral density are related by [51]

$$\langle z^2 \rangle = \int_0^{\infty} S_z(\omega) d\omega = \int_0^{\infty} A\, |G(j\omega)|^2 d\omega, \tag{B20}$$

where $S_z(\omega)$ is the displacement power spectral density ($\mathrm{m}^2\,\mathrm{Hz}^{-1}$) and A can be considered the thermal white noise drive [52]. $G(j\omega)$ is the cantilever transfer function from a force input to displacement output which for the single mode case takes the form [51]

$$|G(j\omega)|^2 = \frac{1/k^2}{\left(1 - \frac{\omega^2}{\omega_0^2}\right)^2 + \frac{\omega^2}{\omega_0^2 Q^2}}. \tag{B21}$$

Using (B19), the mean squared deflection can now be expressed as

$$\langle z^2 \rangle = \int_0^{\infty} A\, |G(j\omega)|^2 d\omega \tag{B22}$$

$$0.8175\frac{k_B T}{k} = A\int_0^{\infty} \frac{1/k^2}{\left(1 - \frac{\omega^2}{\omega_0^2}\right)^2 + \frac{\omega^2}{\omega_0^2 Q^2}} d\omega. \tag{B23}$$

Then, the thermal white noise drive A can be found to be [51–53]

$$A = 0.8175\frac{4m\omega_0 k_B T}{Q}. \tag{B24}$$

Finally, the thermal deflection noise power spectral density as observed by the piezoelectric sensor is obtained as

$$S_z(\omega) = 0.8175\frac{4k_B T}{k\omega_0 Q}\frac{1}{\left(1 - \frac{\omega^2}{\omega_0^2}\right)^2 + \frac{\omega^2}{\omega_0^2 Q^2}}. \tag{B25}$$

Evaluating (B25) at $\omega = \omega_0$ yields the thermal deflections at resonance as observed by the piezoelectric charge sensor

$$N_z(\omega_0) = \sqrt{0.8175\frac{4k_B TQ}{k\omega_0}}. \tag{B26}$$

ORCID iDs

Michael G Ruppert https://orcid.org/0000-0003-2286-4929
Michal Zawierta https://orcid.org/0000-0002-7213-0272
Andrew J Fleming https://orcid.org/0000-0001-7132-8458
Gino Putrino https://orcid.org/0000-0001-6744-865X
Yuen K Yong https://orcid.org/0000-0001-7363-5304

References

[1] Binnig G, Quate C F and Gerber C 1986 *Phys. Rev. Lett.* **56** 930
[2] Binnig G and Rohrer H 1983 *Surf. Sci.* **126** 236
[3] Gentili M, Giovannella C and Selci S (ed) 1994 *Nanolithography—A Borderland between STM, EB, IB, and X-Ray Lithographies* vol 264 (Netherlands: Springer) p 216
[4] Vettiger P *et al* 2002 *IEEE Trans. Nanotechnol.* **1** 39
[5] Giessibl F J 1995 *Science* **267** 68
[6] Minne S, Soh H, Flueckiger P and Quate C 1995 *Appl. Phys. Lett.* **66** 703
[7] Martin Y, Williams C and Wickramasinghe H 1987 *J. Appl. Phys.* **61** 4723
[8] Nievergelt A P, Banterle N, Andany S H, Gönczy P and Fantner G E 2018 *Nat. Nanotechnol.* **13** 696–701
[9] Bhushan B 2010 *Springer Handbook of Nanotechnology* (Berlin: Springer)
[10] Meyer G and Amer N M 1988 *Appl. Phys. Lett.* **53** 1045
[11] García R and Herruzo E T 2012 *Nat. Nanotechnol.* **7** 217
[12] Herruzo E T, Perrino A P and Garcia R 2014 *Nat. Commun.* **5** 3126
[13] Dufrêne Y F, Ando T, Garcia R, Alsteens D, Martinez-Martin D, Engel A, Gerber C and Müller D J 2017 *Nat. Nanotechnol.* **12** 295
[14] Rangelow I W, Ivanov T, Ahmad A, Kaestner M, Lenk C, Bozchalooi I S, Xia F, Youcef-Toumi K, Holz M and Reum A 2017 *J. Vac. Sci. Technol.* B **35** 06G101
[15] Ruppert M G and Moheimani S O R 2016 *Beilstein J. Nanotechnol.* **7** 284
[16] Dukic M, Winhold M, Schwalb C H, Adams J D, Stavrov V, Huth M and Fantner G E F 2016 *Nat. Commun.* **7** 12487
[17] Sarkar N, Lee G, Strathearn D, Olfat M and Mansour R R 2016 *2016 IEEE 29th Int. Conf. on Micro Electro Mechanical Systems (MEMS) (Shanghai, China)* pp 55–8
[18] Ruppert M G, Fowler A G, Maroufi M and Moheimani S O R 2017 *IEEE J. Microelectromech. Syst.* **26** 215
[19] Schneider A, Ibbotson R H, Dunn R J and Huq E 2011 *Proc. 36th Int. Conf. on Micro- and Nano-Engineering (MNE); Microelectron. Eng.* **88** 2390
[20] Kassies R, van der Werf K O, Bennink M L and Otto C 2004 *Rev. Sci. Instrum.* **75** 689
[21] Han W, Lindsay S M and Jing T 1996 *Appl. Phys. Lett.* **69** 4111
[22] Umeda N, Ishizaki S and Uwai H 1991 *J. Vac. Sci. Technol.* B **9** 1318
[23] Yamanaka K and Nakano S 1996 *Japan. J. Appl. Phys.* **35** 3787
[24] Pedrak R, Ivanov T, Ivanova K, Gotszalk T, Abedinov N, Rangelow I W, Edinger K, Tomerov E, Schenkel T and Hudek P 2003 *J. Vac. Sci. Technol.* B **21** 3102
[25] Indermühle P-F, Schürmann G, Racine G-A and de Rooij N 1997 *Sensors Actuators* A **60** 186
[26] Itoh T and Suga T 1993 *Nanotechnology* **4** 218
[27] Tortonese M, Barrett R C and Quate C F 1993 *Appl. Phys. Lett.* **62** 834
[28] Arlett J L, Maloney J R, Gudlewski B, Muluneh M and Roukes M L 2006 *Nano Lett.* **6** 1000
[29] Li M, Tang H X and Roukes M L 2007 *Nat. Nanotechnol.* **2** 114
[30] Dukic M, Adams J D and Fantner G E 2015 *Sci. Rep.* **5** 1
[31] Moore S I, Ruppert M G and Yong Y K 2017 *Beilstein J. Nanotechnol.* **8** 358
[32] Clark J, Hsu W-T, Abdelmoneum M and Nguyen C-C 2005 *IEEE J. Microelectromech. Syst.* **14** 1298
[33] Lee J-Y and Seshia A 2009 *Sensors Actuators* A **156** 36
[34] Lin A-H, Lee J-Y, Yan J and Seshia A 2010 *Sensors Actuators* A **158** 263
[35] Akiyama T, de Rooij N F, Staufer U, Detterbeck M, Braendlin D, Waldmeier S and Scheidiger M 2010 *Rev. Sci. Instrum.* **81** 063706
[36] Coskun M B, Fowler A G, Maroufi M and Moheimani S O R 2017 *IEEE J. Microelectromech. Syst.* **26** 1287

[37] Sadewasser S, Villanueva G and Plaza J A 2006 *Rev. Sci. Instrum.* **77** 073703
[38] Ruppert M G and Yong Y K 2017 *Rev. Sci. Instrum.* **88** 086109
[39] Meitzler A H, Tiersten H F, Warner A W, Berlincourt D and Coquin G A 1988 *ANSI/IEEE Std 176–1987*
[40] Moheimani S O R and Fleming A J 2006 *Piezoelectric Transducers for Vibration Control and Damping* (London: Springer)
[41] Gere J and Timoshenko S 1997 *Mechanics of Materials* (Boston, MA: PWS Publishing Company)
[42] Liu G R and Quek S S 2003 *Finite Element Method: A Practical Course* (Amsterdam: Elsevier)
[43] Ruppert M G and Moheimani S O R 2013 *Rev. Sci. Instrum.* **84** 125006
[44] Cowen A, Hames G, Glukh K and Hardy B 2014 *PiezoMUMPs Design Handbook* 1st edn (Durham: MEMSCAP Inc.)
[45] Sader J E, Sanelli J A, Adamson B D, Monty J P, Wei X, Crawford S A, Friend J R, Marusic I, Mulvaney P and Bieske E J 2012 *Rev. Sci. Instrum.* **83** 103705
[46] Fukuma T, Kimura M, Kobayashi K, Matsushige K and Yamada H 2005 *Rev. Sci. Instrum.* **76** 053704
[47] Lévy R and Maaloum M 2002 *Nanotechnology* **13** 33
[48] Hutter J L and Bechhoefer J 1993 *Rev. Sci. Instrum.* **64** 1868
[49] De Silva C W 2000 *Vibration-Fundamentals and Practice* (Boca Raton, FL: CRC Press)
[50] Butt H J and Jaschke M 1995 *Nanotechnology* **6** 1
[51] Albrecht T, Grütter P, Horne D and Rugar D 1991 *J. Appl. Phys.* **69** 668
[52] Heer C V 1972 *Statistical Mechanics, Kinetic Theory, and Stochastic Processes* (New York: Academic)
[53] Shusteff M, Burg T P and Manalis S R 2006 *Am. J. Phys.* **74** 873